Chapter 9
Neutron Scattering of Proton-Conducting Ceramics

Maths Karlsson

Abstract This chapter aims to demonstrate the important role that neutron scattering now plays in advancing the current understanding of the basic properties of proton-conducting ceramic separator-materials for future intermediate-temperature fuel cells. In particular, the breadth of contemporary neutron scattering work on proton-conducting perovskite-type oxides, hydrated alkali thio-hydroxogermanates, solid acids, and gallium-based oxides, is highlighted to illustrate the range of information that can be obtained. Crucial materials properties that are examined include crystal structure, proton sites, hydrogen bonding interactions, proton dynamics, proton concentrations, and nanoionics. Furthermore, the prospectives for future neutron studies within this field, particularly in view of the latest developments of neutron methods and the advent of new sources and their combination with other techniques, are discussed.

9.1 High-Temperature Fuel Cells and the Strive Towards Intermediate Temperatures

A particularly promising, yet challenging, clean-energy technology is the solid oxide fuel-cell (SOFC) [1–9]. At the heart of this device is an oxide-ion or proton-conducting oxide electrolyte, which is sandwiched between two porous electrodes (the anode and cathode). The working principle of the SOFC is based on the chemical reaction of hydrogen (at the anode) and oxygen (at the cathode) to produce electricity and water, working temperatures being in the range ~800–1,000 °C. The electrolyte does not conduct electrons, but is permeable to the diffusion of either oxide ions or protons. Schematics of SOFCs based on oxide-ion and proton-conducting electrolytes are shown in Fig. 9.1.

M. Karlsson (✉)
Chalmers University of Technology, 412 96 Göteborg, Sweden
e-mail: maths.karlsson@chalmers.se

G.J. Kearley and V.K. Peterson (eds.), *Neutron Applications in Materials for Energy*, Neutron Scattering Applications and Techniques,
DOI 10.1007/978-3-319-06656-1_9

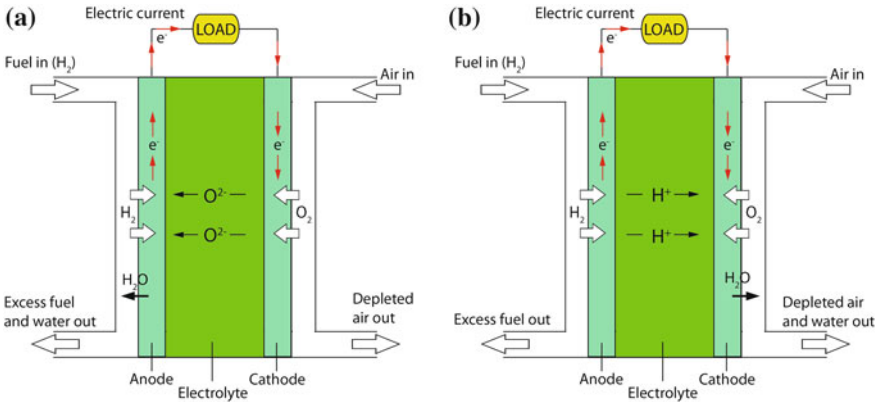

Fig. 9.1 Schematics of the operation of a SOFC utilizing **a** oxide-ion and **b** proton-conducting electrolyte

In the 1990s the Siemens Westinghouse SOFC, consisting of an oxide-ion conducting yttria-stabilized zirconia (YSZ) electrolyte, a lanthanum strontium manganite cathode, and a nickel-YSZ cermet anode, in a unique tubular design, was developed and is now commercially available [1, 10, 11]. Thanks to its high operation temperature, which offers the advantages of fuel flexibility (existing fossil fuels can be used) and high energy-conversion efficiency, the SOFC is particularly attractive for use in combined heat and power applications or efficiently coupled with gas turbines. However, the high operation-temperature also has disadvantages, such as a long startup time, durability issues, and the need for relatively expensive component materials. Therefore, in more recent years, much research has focused on trying to reduce the operation temperature of the SOFC to the so-called *intermediate temperature range* between approximately 200 and 500 °C. Such a reduction in operating temperature would have a beneficial impact on the total cost and the durability of the fuel cell, as problems associated with thermal cycling and performance degradation would be reduced and it would be possible to use cheaper materials in interconnects and heat exchangers [12]. Lowering the temperature would also shorten the startup time of the fuel cell, which is of particular importance for mobile applications. Further, in comparison to low temperature (<100 °C) polymer-electrolyte membrane fuel cells (PEMFCs) [13], a temperature of 200 °C is high enough in order to allow for the use of smaller amounts of expensive platinum to catalyze the electrode reactions [12]. In fact, intermediate-temperature fuel-cell technology has the unique potential to be used both for stationary combined heat and power systems and for hybrid and plug-in hybrid vehicles and are indeed expected to produce energy densities per volume and specific energy per weight significantly larger than state-of-the-art Li ion and Ni metal hydride batteries [14].

However, it is discouraging that any decrease of the operation temperature of SOFCs results in a decreased power density of the device, mainly due to a lowering of the ionic conductivity of the electrolyte. Targeted conductivities exceed

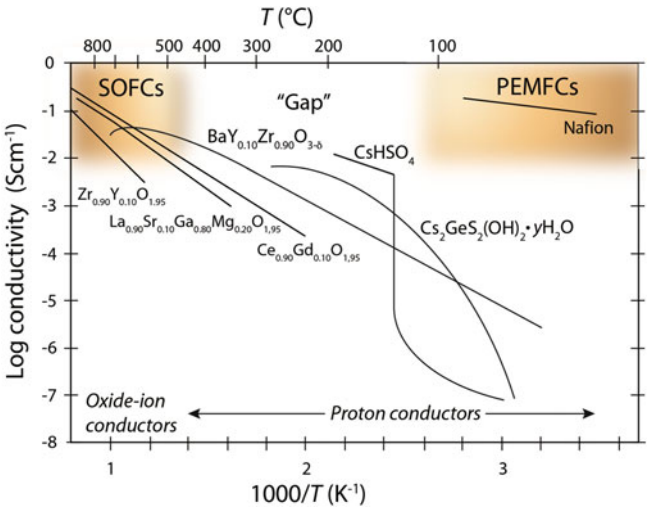

Fig. 9.2 Conductivity of state-of-the-art electrolytes over a wide temperature range. Note the gap of highly-conducting materials in the temperature range ~100–500 °C. The figure is redrawn and modified from Ref. [15], copyright Wiley, 2002. The conductivity of $Cs_2GeS_2(OH)_2{\cdot}yH_2O$ is taken from Ref. [16]

0.01 Scm^{-1},[1] and in this respect proton-conducting ceramics emerge as the main candidate electrolytes for SOFCs. However, despite intense research, the conductivities of even the best proton-conducting ceramics are still one to two orders of magnitude below the target. This can be appreciated from Fig. 9.2, which displays the conductivities for the state-of-the-art ionic conductors over a wide temperature range, including electrolytes for low temperature PEMFCs and high-temperature SOFCs, i.e. the more mature fuel-cell technologies. A significant advancement in relation to the conductivity of present day proton-conducting ceramics is therefore critical to future breakthroughs in the development of next-generation fuel-cell technology, operating in the intermediate temperature range. Such an enhancement depends on increasing the understanding of the fundamental science of key materials aspects such as crystal structure and proton-conduction mechanisms, in the most promising classes of materials, and the exploration of novel and completely new systems. For this purpose, neutron scattering is a powerful tool that has been applied successfully to studies of both oxide-ion and proton-conducting materials, and its role in this area of research is vast.

[1] To ensure that the total internal resistance (electrolyte + electrodes) of a fuel cell is sufficiently small, the target value for the areal specific-resistivity of the electrolyte is set at 0.15 Ωcm^2. Oxide films can be reliably produced using conventional ceramic fabrication routes at thicknesses down to ~15 μm. It follows that the specific conductivity of the electrolyte must exceed 0.01 Scm^{-1} [1].

The aim of this chapter is not to give an exhaustive account for all the neutron scattering studies in this field, nor is it aimed at providing a review of SOFC technology, as excellent reviews can be found elsewhere [1–9]. Rather, this chapter centres on proton-conducting ceramics as separator materials for intermediate-temperature fuel cells and aims to give a flavour of how a variety of neutron methods can be used to reveal the details of structures and proton dynamics in this class of energy-relevant materials. In particular, the scope of contemporary structural and dynamical studies of *perovskite-type oxides*, known as the most promising class of proton-conducting ceramics for intermediate temperature fuel-cell applications, will be reviewed. This is followed by a concise review of selected examples of studies of other classes of promising candidate materials, such as hydrated alkali thio-hydroxogermanates, solid acids, and lanthanum gallates, to illustrate the breadth of information that can be obtained. The chapter finishes with my personal thoughts on prospectives for future work in this timely area of research. The chapter may be viewed as an extended version of my recent publication in Dalton Trans. [17].

9.2 Proton-Conducting Perovskites

The first report on proton conduction in perovskite-structured oxides dates back to 1981, when Iwahara and co-workers [18] showed that the perovskites $SrCeO_3$ and $BaCeO_3$ exhibit high proton-conductivities in hydrogen-containing atmospheres and may be applicable as electrolytic membrane in electrochemical cells such as fuel cells, steam electrolyzers, and gas sensors. Although $BaCeO_3$ has remained a benchmark for high proton-conductivity in perovskites, many other related materials have been developed and found to be proton conducting. Examples include more complex perovskites such as $Ba_3Ca_{1.18}Nb_{1.82}O_{8.73}$ [19–21], rare earth oxides such as Er_2O_3 [22], and pyrochlore-type oxides such as $La_2Zr_2O_7$ [23, 24].

9.2.1 The Perovskite Structure

The basic chemical formula of perovskite-type oxides is ABO_3, where *A* represents a relatively large cation with oxidation state +1, +2, or +3, and *B* is a cation with oxidation state between +1 and +7. For proton-conducting perovskites, *A* is usually +2 (e.g. Sr^{2+} or Ba^{2+}) and *B* is usually +4 (e.g. Ce^{4+} or Zr^{4+}). The "ideal" perovskite structure is defined by a cubic lattice of corner-sharing BO_6 octahedra and 12-fold coordinated *A* site ions, see Fig. 9.3a. A cubic structure is, however, typically observed only if the sizes of the cations are compatible with the sizes of their respective interstices, and if not, the perovskite adopts a structure of lower symmetry. The deviation from cubic symmetry may be quantified with the

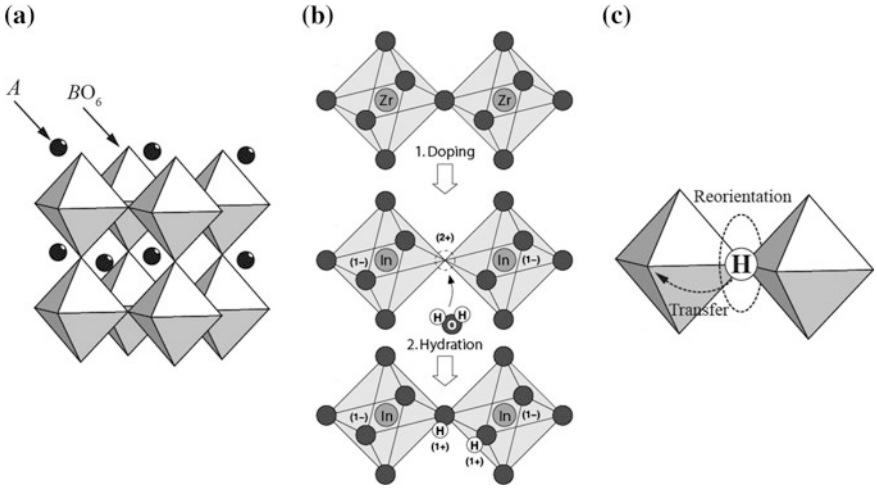

Fig. 9.3 **a** Schematic of the cubic ABO_3-type perovskite structure showing the octahedrally coordinated B^{4+} ions within BO_6 octahedra and the 12-fold coordinated A^{2+} ions. **b** Schematic of doping with In^{3+} at the Zr^{4+} site in cubic-structured $BaZrO_3$, followed by the incorporation of protons through hydration in a humid atmosphere. **c** Schematic of the two principal steps of the proton-conduction mechanism in hydrated perovskites

Goldschmidt factor, t_G, which has a value of one or close to one for a cubic perovskite [25].[2]

9.2.2 The Incorporation of Protons

Loading protons into the perovskite structure depends on acceptor doping at the *B* site [26]. Acceptor doping, such as when In is substituted for Zr in $BaZrO_3$, creates an oxygen-deficient structure, which under elevated temperature and humidity absorbs water dissociatively so that oxygen vacancies fill with hydroxyl groups and the remaining protons bind to other oxygens in the structure [26]. In the Kröger-Vink notation [27] this reaction is written

$$H_2O + V_O^{\cdot\cdot} + O_O^{\times} \Leftrightarrow 2(OH_O^{\cdot}), \tag{9.1}$$

where $V_O^{\cdot\cdot}$ denotes an oxygen vacancy, $O_O^{\times}$ denotes a lattice oxygen, and $OH_O^{\cdot}$ denotes a proton bound to a lattice oxygen (the superscripts $\cdot$ and $\times$ denote positive and neutral charges, respectively). The protonation process is shown schematically

[2] $t_G = (R_A + R_O)/\sqrt{2}(R_B + R_O)$, where R_A is the ionic radius of the *A* ion, R_B is the ionic radius of the *B* ion, and R_O is the ionic radius of oxygen [25].

in Fig. 9.3b. At elevated temperature, the protons are not stuck to any particular oxygen but move rather freely from one oxygen to another, as described further below, resulting in a high conductivity of the material.

9.2.3 Proton Mobility

The dynamical picture of the proton-conduction mechanism in hydrated perovskites started to emerge in the mid-nineties and is mainly based on results obtained from molecular-dynamics simulations [28–31] and quasielastic neutron scattering [32, 33]. On a local scale, the protons jump between neighbouring oxygens, with an intermediate reorientational motion of the −OH group in between jumps (a schematic is shown in Fig. 9.3c), whereas at the longer length-scale the protons diffuse as a series of such jumps and reorientations. However, the effect of dopant atoms on the local chemistry and structure, as well as the resultant symmetry reduction and proton-defect interactions, complicate the description of the proton conductivity and such effects are not completely understood for even the simplest perovskite systems.

A key parameter for long-range proton diffusion is the hydrogen bonding experienced between a proton and a neighbouring oxygen, since the transfer between neighbouring oxygens is a hydrogen-bond mediated process, whereas the reorientational motion of the −OH group requires the breaking of such bonds. The proton diffusivity is further affected by the vibrational dynamics of the proton. More specifically, the proton performs localized O–H stretch and O–H wag vibrations, which may be seen as precursors to the transfer and reorientational step, respectively. There is also a coupling of the proton motions to the phonons of the perovskite host lattice [30, 34]. Hence, the hydrogen bonding, vibrational dynamics, and long-range proton diffusion are, most likely, strongly correlated.

9.2.4 State-of-the-Art of Proton-Conducting Perovskites

The highest proton-conductivities in polycrystalline samples of perovskite-structured oxides are generally found in barium cerates ($BaCeO_3$-based compounds), however, these materials react with CO_2 and/or H_2O at intermediate temperatures to form $BaCO_3$ (or $Ba(OH)_2$) and CeO_2 and therefore degrade with time. Hence, they are poorly suited for use in fuel cells [26]. Strategies to increase the chemical stability of such materials include substitution (doping) of different types of atoms, but improvements are generally small. In comparison, barium zirconates ($BaZrO_3$-based compounds) show excellent chemical stability in CO_2 and H_2O-containing atmospheres and are in this respect more suitable for use in fuel cells from an

application point of view. The conductivity of one specific barium zirconate, namely 10 % Y-doped $BaZrO_3$ (included in Fig. 9.2), indeed exhibits the highest bulk proton-conductivity reported for any oxide material [26]. However, barium zirconates are difficult to sinter, which implies that barium zirconate samples contain a relatively-large volume of grain boundaries, which decrease the total conductivity [26, 35–38]. The sinterability of barium zirconates may be enhanced with the use of sintering aids [36, 39] or by the introduction of a second dopant at the *B* site of the perovskite [40, 41], however, the bulk conductivity is then typically lowered.

9.3 Neutron Scattering of Proton-Conducting Perovskites

The development of new perovskite structures with improved conductivity, thermodynamical stability, and sinterability, depends on the exploration of new classes of compounds as well as an increased understanding of the basic science of those materials already known. Such investigations should elucidate key material detail such as crystal structure, proton sites, proton concentrations, hydrogen-bonding interactions, and the mechanics of proton dynamics on different time- and length-scales, as well as to clarify how these details correlate with each other. For this purpose, neutron scattering offers the unique potential to access simultaneously information in both space and time, through the momentum ($\hbar Q$) and energy ($\hbar E$) transferred in the scattering event, respectively. This combination makes neutron scattering a powerful tool for investigating structures (using neutron diffraction (ND)), vibrational dynamics and hydrogen-bonding interactions (using inelastic neutron scattering (INS)), and diffusional dynamics (using quasielastic neutron scattering (QENS)). Neutrons can also be used to obtain details concerning the proton concentration in the sample through prompt-gamma activation analysis (PGAA). Therefore, neutrons offer good opportunities to advance the understanding of state-of-the-art proton-conducting perovskites. In this context, the remainder of this chapter aims to give a flavour of the important role that neutron methods play in providing a deep insight into the functionality of these materials. Emphasis is put on barium zirconates, due to their great promise for fuel-cell applications.

Examples of recent neutron work on proton-conducting perovskites, which are here briefly reviewed, include studies of proton sites and local structures using ND (Sect. 9.3.1), studies of vibrational proton dynamics and hydrogen-bonding interactions using INS (Sect. 9.3.2), studies of proton diffusion using QENS (Sect. 9.3.3), and studies of proton concentrations using PGAA (Sect. 9.3.4). No attempt has been made to be complete in this work, with the aim rather to highlight the different types of information that can be obtained using neutrons.

9.3.1 Neutron Diffraction

ND has been widely applied to study proton-conducting perovskites. More frequently, Rietveld refinement using *conventional* neutron powder diffraction data is applied, and in some cases, is used to understand how the structure may change with temperature and/or surrounding atmosphere. ND is of paramount importance for studies of proton-conducting perovskites due to its ability to determine proton sites, with both Rietveld and pair-distribution function (PDF) analysis of neutron total-scattering data being applied.

9.3.1.1 Determination of Proton Sites

Knowledge about proton sites is essential to understand the properties of proton-conducting oxides, whether it be the local proton-dynamics, hydrogen-bonding interactions, or macroscopic proton-conductivity. Some early examples of ND measurements on proton-conducting perovskites in this area include by Knight [42] who reported on $BaCe_{0.9}Y_{0.1}O_{2.95}$, Sata et al. [43] who reported on Sc-doped $SrTiO_3$, Sosnowska et al. [44] who reported on $Ba_3Ca_{1.18}Nb_{1.82}O_{9-\delta}$, and Kendrick et al. [45] who reported on $La_{0.6}Ba_{0.4}ScO_{2.8}$. More recently, Ahmed et al. [46] reported on $BaZr_{0.50}In_{0.50}O_{3-\delta}$, whilst Azad et al. [47] reported on $BaCe_{0.4}Zr_{0.4}Sc_{0.2}O_{2.9}$. One may note that most of these studies were performed on samples which were deuterated rather than hydrated, in order to reduce the incoherent scattering and transform the scattering into a useful signal, which increases the chance of locating the positions of protons even in systems with low proton-concentration.

To give a representative example of the previous work we turn to the neutron powder diffraction measurements by Ahmed et al. [46] on $BaZr_{0.50}In_{0.50}O_{3-\delta}$. As pointed out by the authors, the Rietveld analysis of the ND patterns (Fig. 9.4a) indicated no departure from cubic $Pm\bar{3}m$ symmetry. However, further analysis showed that the material is phase-separated into a deuterium-rich and non-deuterated phase with phase fractions of 85 and 15 %, respectively.

To determine the deuterium positions in the deuterium-rich phase, the authors calculated the Fourier-difference maps by taking the difference between simulated (with no deuterium in the structural model) and experimental data in reciprocal space; the Fourier-difference map taken at $z = 0$ is shown in Fig. 9.4b. Here, the positive peak at approximately (0.5, 0.2, 0) in Fig. 9.4b is consistent with the positive scattering-length of deuterium, suggesting that this is the deuterium site. However, from a closer analysis of the neutron data, it was found that the missing scattering density is distributed anisotropically within the *ab* plane, which suggests instead delocalization of the deuterium atom at the 24*k* site. It follows that there are eight equivalent deuterium-sites around each oxygen, which are tilted towards a neighbouring oxygen [46]. Such tilting increases the tendency for the formation of a strong hydrogen-bond between the deuterium and the oxygen towards which it is

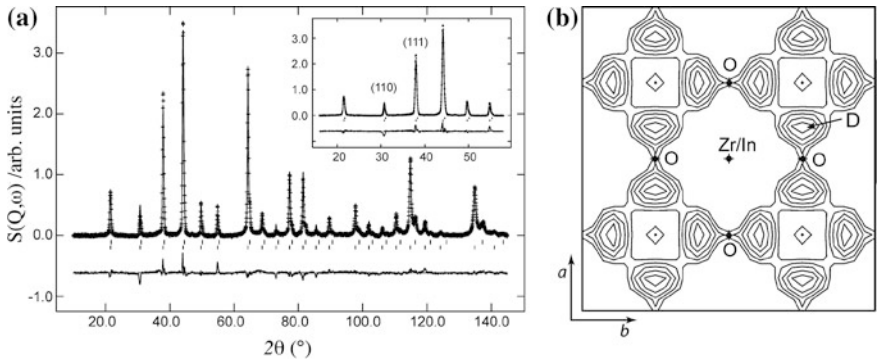

Fig. 9.4 **a** ND pattern for deuterated $BaZr_{0.50}In_{50}O_{3-\delta}$, obtained on the D2B instrument at the Institut Laue-Langevin in Grenoble, France, as reported by Ahmed et al. [46]. Crosses are experimental data, lines are calculated and difference plots (through the data and at the bottom, respectively). The lower set of tick marks indicates the position of calculated reflections for the deuterated phase with no deuterium position defined in the structural model, whereas the upper set of tick marks are those of the non-deuterated phase. The inset shows a close-up of the significant discrepancies between calculated and observed intensities reflecting the absence of D in the structural model. **b** Fourier-difference maps taken at $z = 0$, showing missing positive scattering-density attributed to D. The positive peak, marked as D, is located at approximately (0.5, 0.2, 0). Map size from centre of edge is set to the unit-cell parameter, ~4.2 Å. Contour lines are drawn at 0.0132, 0.0264, 0.0396, 0.0528, and 0.0660 fm $Å^{-1}$. Reprinted with permission from (I. Ahmed, C.S. Knee, M. Karlsson, S.G. Eriksson, P.F. Henry, A. Matic, D. Engberg,L. Börjesson, J. Alloy Compd. **450**, 103 (2008)) Ref. [46], copyright Elsevier

tilted (*c.f.* Fig. 9.5a) and is consistent with results obtained both from first-principles calculations and infrared spectroscopy [48].

Further structural refinements based on the diffraction patterns revealed highly-anisotropic atomic displacement parameters (ADPs) of the oxygen atoms, as illustrated in Fig. 9.5b, as well as the deuterium site occupancy. The large ADPs

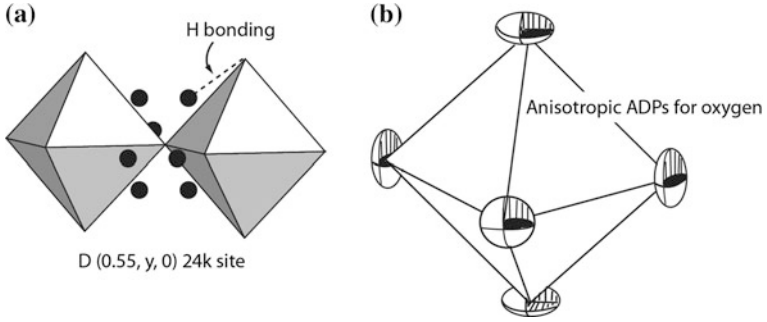

Fig. 9.5 **a** Representation of the refined 24*k* structural site for the deuteron in the deuterium-rich phase of the deuterated sample of $BaZr_{0.50}In_{0.50}O_{3-\delta}$ at 5 K. **b** Schematic picture of the ADPs of oxygen ions in deuterated $BaZr_{0.50}In_{0.50}O_{3-\delta}$. Reprinted with permission from (I. Ahmed, C.S. Knee, M. Karlsson, S.G. Eriksson, P.F. Henry, A. Matic, D. Engberg,L. Börjesson, J. Alloy Compd. **450**, 103 (2008)) Ref. [46], copyright Elsevier

reflect static, localized, displacements of the oxygen ions around their ideal site in a cubic structure and most likely result from the structural disorder as induced by the difference in size between Zr^{4+} and In^{3+} [46]. Similarly, large ADPs have been obtained elsewhere for the composition $BaZr_{0.33}In_{0.67}O_{3-\delta}$ and those results were also attributed to static-disorder effects [49]. To conclude, the authors not only succeeded in determining the location and concentration of protons (deuterons) in the perovskite structure, but also revealed the presence of pronounced short-range structural distortions of the average cubic perovskite-structure, which are likely to affect considerably the proton transport in the material. More detailed information about the local structure, however, needs the use of more local probes, such as PDF analysis of neutron total-scattering data, which is highlighted below.

9.3.1.2 Local Structural Studies with Neutron Total Scattering

The "extra" scattering between Bragg peaks adds information about the structure on a local scale and is therefore of high importance for structural studies of proton-conducting perovskites when the material is not fully periodic, such as when disorder is present. In particular, the pair-correlation function $G(r)$ is sensitive to key structural details, such as bond distances and angles, the symmetry of structural distortions, and oxygen and/or cation ordering, for example. The initial neutron total-scattering experiments coupled to PDF analysis of proton-conducting perovskites were done by Malavasi et al. [50, 51] on undoped and Y-doped $BaCeO_3$. For the undoped material, the neutron total-scattering data suggests no difference between the long-range orthorhombic *Pnma* structure as determined by Rietveld refinement and the short-range structure as determined from PDF analysis, regardless if the sample is hydrated or not [51].

The good agreement between the long-range and short-range structures may be appreciated from Fig. 9.6, which, for the dry undoped material, shows the good fit of the *Pnma* model obtained from Rietveld refinement to $G(r)$. For the dry Y-doped material, however, the fit of the *Pnma* model is less satisfactory, *c.f.* Fig. 9.7a. For this material, the authors instead found an excellent agreement between the $G(r)$ and a structural model based on the lower-symmetry space group $P2_1$ (see Fig. 9.7b), indicating local regions around the Y dopant of such symmetry [51]. Moreover, it was found that the Y-doped material returns to the orthorhombic *Pnma* structure upon hydration, suggesting that the source of local structural distortion is mainly due to Y-induced oxygen vacancies and not linked directly to the substitution of cations [51]. Since the local structure around the proton can be expected to correlate strongly with the mechanistic detail of proton dynamics, such local structural information is of high interest and indeed crucial for the tailoring of new materials with higher proton-conductivities. The importance of understanding the details of local structure may be exemplified by the 10 % Y- and Sc-doped $BaZrO_3$ materials, which both exhibit an *average* cubic structure, but for which the proton conductivity differs by several orders of magnitude [52].

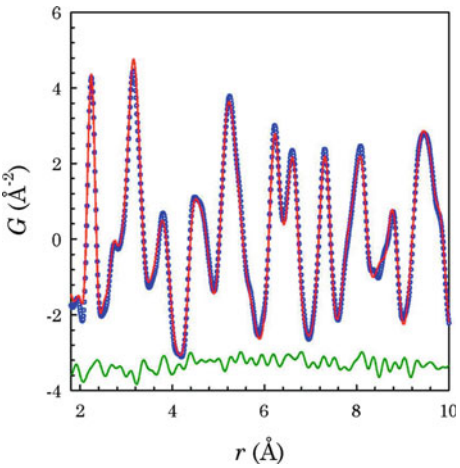

Fig. 9.6 Fit of the pair-correlation function of dry $BaCeO_3$, using the *Pnma* model obtained from Rietveld refinement. *Blue circles* represent the experimental data, the *red line* the calculated data, and the *green line* the difference between the two. Reprinted with permission from (L. Malavasi, H.J. Kim, T. Proffen, J. Appl. Phys. **105**, 123519 (2009)) Ref. [51], American Institute of Physics

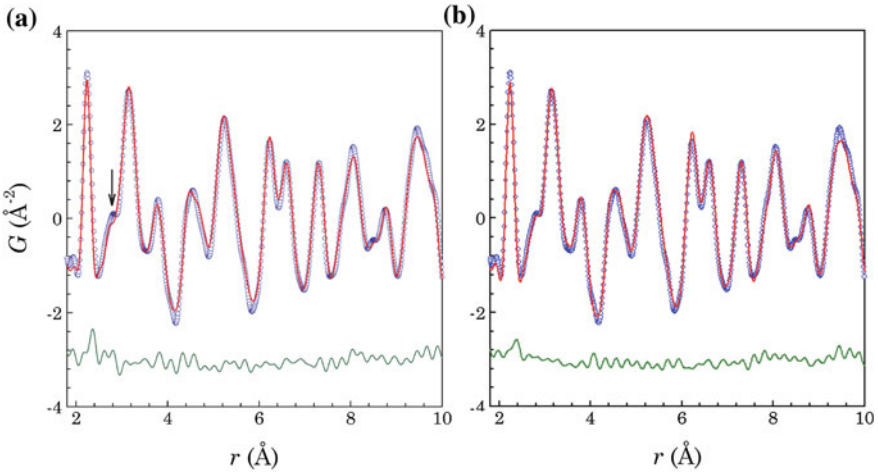

Fig. 9.7 Fit to $G(r)$ of dry Y-doped $BaCeO_3$, using a *Pnma* model **a** and $P2_1$ model **b**. Regions with a marked difference between experimental data (*blue line*) and calculated quantity (*red line*) are highlighted with *arrows*. Note the better agreement when using the $P2_1$ model. The *green line* is the difference between the model and the calculation. Reprinted with permission from (L. Malavasi, H.J. Kim, T. Proffen, J. Appl. Phys. **105**, 123519 (2009)) Ref. [51], American Institute of Physics

9.3.2 *Inelastic Neutron Scattering Studies of Vibrational Proton-Dynamics*

The first INS study on proton-conducting perovskites was done by Karmonik et al. [53] who investigated vibrational proton-dynamics in $SrCe_{0.95}M_{0.05}O_{3-\delta}$ (M = Sc, Ho, Nd). The INS spectra of the materials are reprinted in Fig. 9.8a and reveal O–H wag modes at around 115 (Sc) and 105 (Ho) meV. For the Nd-doped equivalent, the O–H wag band overlaps with a band at ~80 meV. It appears that the frequency of the O–H wag mode shifts to higher wavenumbers with decreasing size of the dopant cation (Nd → Ho → Sc), indicating that this band is related to protons in the vicinity of such atoms [53]. This behaviour was later validated by Yildrim et al. [54], who performed lattice-dynamics calculations on a $\sqrt{2} \times \sqrt{2} \times 1$ supercell of $SrCeO_3$, replacing one Ce by Sc + H to give a supercell of $Sr_8Ce_7ScHO_{24}$, whose composition is close to that of the real material. In particular, the authors calculated the vibrational spectrum for the hydrogen at the undoped (U) and doped (D) site and by comparing the experimental and calculated spectra (Fig. 9.8b) it could be confirmed that the O–H wag mode at ~120 meV indeed is associated with protons close to dopant (Sc) atoms, whereas the O–H wag mode at lower frequency, ~80 meV, is associated with protons in the vicinity of host-lattice Ce atoms [54].

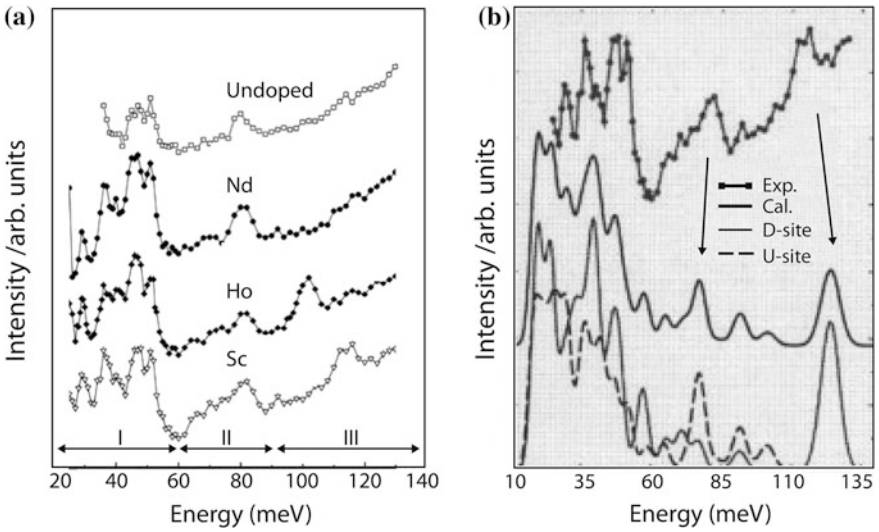

Fig. 9.8 **a** INS spectra of hydrated samples of $SrCeO_3$ and $SrCe_{0.95}M_{0.05}O_{3-\delta}$ (M = Sc, Ho, Nd), revealing three well-defined vibrational bands in the energy ranges 20–60, 60–90, and 100–140 meV. **b** Comparison of the INS spectrum of hydrated $SrCe_{0.95}M_{0.05}O_{3-\delta}$ (*top*) and the calculated spectrum of $Sr_8Ce_7ScHO_{24}$. *Lines* shown at the *bottom* are the contributions from the H–MO_6 clusters, where M = Ce (U site) and M = Sc (D site). The figure is modified and reprinted with permission from (T. Yildrim, B. Reisner, T.J. Udovic, D.A. Neumann, Solid State Ionics **145**, 429 (2001)) Ref. [54], copyright Elsevier

More recently, Karlsson et al. [55] addressed the question of how the O–H wag frequency depends on the dopant concentration. Specifically, the authors performed a systematic INS study of the $BaIn_xZr_{1-x}O_{3-x/2}$ ($x = 0.20$, 0.50, and 0.75) system, which exhibits an average cubic $Pm\bar{3}m$ symmetry independent of the In concentration. The INS spectra are shown in Fig. 9.9a. It can be seen that the O–H wag vibrations show up as a strong, broad, band between approximately 600 and 1,300 cm^{-1}, whilst the peak-fit analysis presented in Fig. 9.9b shows that this band can be decomposed into three Gaussian components. Figure 9.9c shows the In concentration dependence of the relative intensities of the three peak fitted Gaussians. A significant redistribution of intensity amongst the three Gaussians as the In concentration is varied can be observed (the total integrated-intensity of the O–H wag band increases linearly with increasing In concentration [55]). Most interestingly, there is an increased contribution from the two high-frequency components to the overall spectrum, reflected by a band broadening towards higher frequencies, whereas the width and position of each individual Gaussian are found to be essentially independent of the In concentration [55]. The increase in total intensity of the O–H wag band results from the increasing concentration of protons in the sample, whereas the increased contribution of the high-frequency modes is due to an increased fraction of protons in more or less strongly hydrogen-bonding configurations [55]. The formation of strong hydrogen-bonds is believed to be the result of dopant atoms and/or oxygen vacancies in the vicinity of the protons, which act as charged defects, pushing the proton towards a neighbouring oxygen and increasing the tendency for hydrogen-bond formation [55]. However, the presence of such strongly hydrogen-bonding configurations may equally well be the result of tilts and/or rotations of oxygen octahedra induced by doping at the acceptor-atom site, which is of purely static origin [56]. Whatever the case, the formation and breaking of hydrogen bonds are crucially important for long-range proton transport, since proton transfer is a hydrogen-bond mediated process. Thus, information about the nature of hydrogen bonds, which can be derived from the O–H stretch and O–H wag frequencies, and how they link to the structural and dynamical details of the material, is highly valuable. Moreover, O–H stretch and O–H wag mode frequencies are useful in computer simulations, where they are utilized as prefactors in transition-state models to estimate the rates of proton transfer and −OH reorientational motion, respectively [57].

Further information about the behaviour of protons in the perovskite lattice may be derived from the temperature dependence of the INS spectra. In this regard, Karlsson et al. [55] performed a variable-temperature study on $BaZr_{1-x}In_xO_{3-x/2}$ ($x = 0.20$). The INS spectra measured at $T = 30$, 100, 200, and 300 K are shown in Fig. 9.9d. As can be seen the spectra measured at the four different temperatures look essentially the same, which suggests that there is only a small change of the Debye-Waller factor as the temperature is raised from 30 to 300 K, i.e. the total root mean-square displacement, U_T, increases only slightly within this temperature range [55]. The weak temperature-dependence of U_T indicates that there is no particular difference between the proton dynamics in this material at 30 and 300 K.

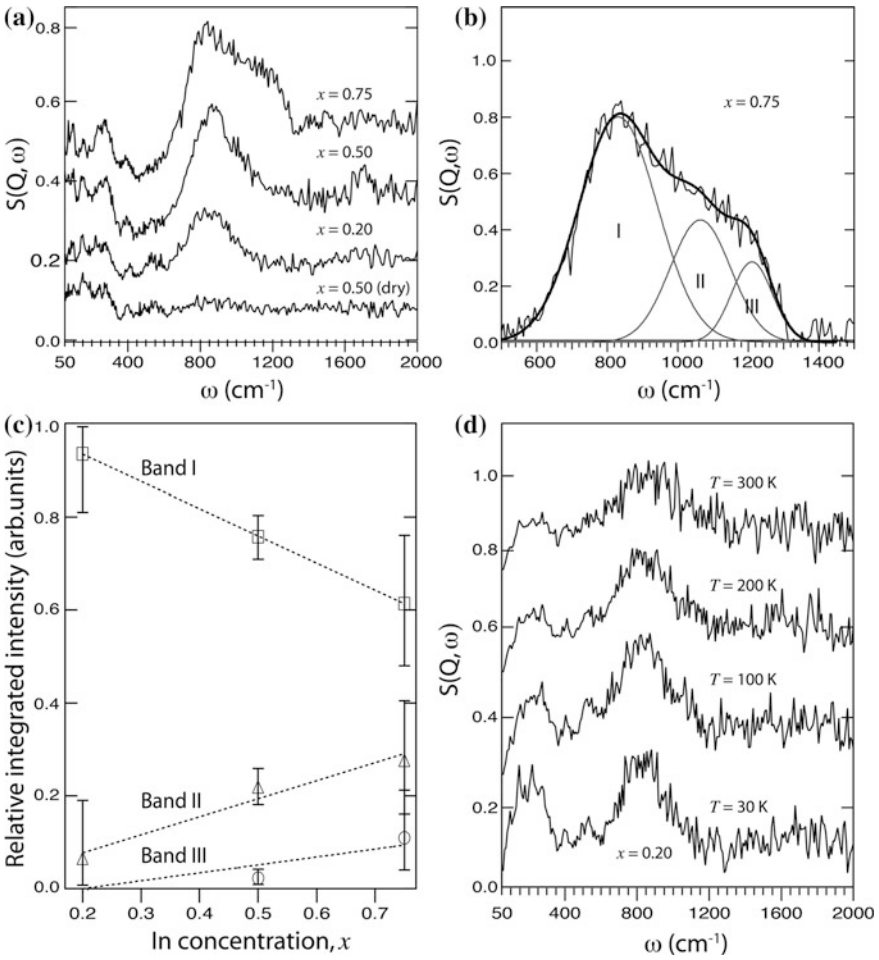

Fig. 9.9 **a** INS spectra for hydrated and dry samples of the $BaIn_xZr_{1-x}O_{3-x/2}$ ($x = 0.20$, 0.50, and 0.75) perovskite system, measured at $T = 30$ K. **b** Peak fit of the baseline-corrected spectrum of $BaIn_xZr_{1-x}O_{3-x/2}$ ($x = 0.75$). **c** Relative integrated-intensities of the three Gaussian components as a function of x. Lines are linear fits and serve as guides for the eye. **d** The INS spectrum of $BaIn_xZr_{1-x}O_{3-x/2}$ ($x = 0.20$) shown for T = 30, 100, 200, and 300 K. The spectra have been separated vertically. Reprinted with permission from (M. Karlsson, A. Matic, S.F. Parker, I. Ahmed, L. Börjesson, S.G. Eriksson, Phys. Rev. B **77**, 104302 (2008)) [55], copyright American Physical Society

Since it is unlikely that the protons undergo long-range diffusion at 30 K, it follows that this is also the case at 300 K. This is in agreement with the generally low proton-conductivity for barium zirconates at these temperatures [26, 52].

9.3.3 Quasielastic Neutron Scattering

Quasielastic neutron scattering (QENS) has played a central role in understanding the nature of proton dynamics in proton-conducting perovskites. The usefulness of the technique comes from the fact that it gives access to the relevant time- and length-scales on which the atomic-scale dynamics of protons typically occur. In addition, the very large neutron-scattering cross section of protons provides a good contrast in experiments and enables studies of systems containing only small amounts of protons.

9.3.3.1 Studies of Local-Diffusional Proton-Dynamics

The majority of QENS studies on proton-conducting perovskites have been performed with the use of either time-of-flight or backscattering methods [58]. These methods give access to the picosecond timescale, extended to ~ 1 nanosecond in some cases, in which local diffusional-dynamics have been observed, although data have also been interpreted in terms of translational diffusion [59, 60]. The first work was done by Hempelmann et al. [32, 33] for $SrYb_{0.05}Ce_{0.95}O_{2.975}$, where rotational-diffusional motion of the $-OH$ group was observed. These results gave support for molecular-dynamics simulations, which suggested that the proton-conduction mechanism in hydrated perovskites involves proton jumps between neighbouring oxygens and rotational diffusion of the $-OH$ group between proton transfers [28–31]. Later, Groß et al. [61] reported on localized diffusional proton-dynamics in $BaZr_{0.85}M_{0.15}O_{2.925}$ (M = Y, In, and Ga), Pionke et al. [59] reported the proton self-diffusion constant for protons in $Ba[Ca_{0.39}Nb_{0.61}]O_{2.91}$, and similarly, Wilmer et al. [62] presented results for $BaY_{0.10}Zr_{0.90}O_{2.95}$. Braun et al. [60], reported two different activation energies for proton diffusion in $BaY_{0.10}Zr_{0.90}O_{2.95}$ at different temperature ranges, Colomban et al. [63] reported a change in local proton-dynamics across a structural phase transition of $(Ba/Sr)Zr_{1-x}Ln_xO_{3-\delta}$, whilst Karlsson et al. [64] reported a relatively-small difference in the activation energy for local proton-dynamics depending on the choice of dopant atom in $BaM_{0.10}Zr_{0.90}O_{2.95}$ (M = Y and Sc). This collection of examples illustrates the success of time-of-flight and backscattering methods to study the local diffusional proton-dynamics in proton-conducting oxides. However, to reach the long time-scale of several nanoseconds needed to study the long-range translational proton-diffusion on an atomic length-scale ($\sim$1–30 Å), another QENS method, namely neutron spin-echo (NSE) spectroscopy, is required.

9.3.3.2 Studies of Long-Range Diffusional Proton Dynamics

NSE offers a unique opportunity to obtain information about dynamical processes on different timescales, e.g. from the elementary processes of the proton-conduction mechanism occurring on the picosecond timescale to the long-range translational

diffusion of protons occurring on the nanosecond timescale, simultaneously. Despite these advantages, the first application of NSE to investigate proton-conducting ceramics was relatively recent, in 2010 when Karlsson et al. [65] reported proton dynamics in hydrated $BaY_{0.10}Zr_{0.90}O_{2.95}$. Figure 9.10a shows the intermediate-scattering function, $I(Q,t)$, at different temperatures (521–650 K) at the Q-value of 0.3 $Å^{-1}$, within the time-range of 0.2–50 ns. The $I(Q,t)$ is characterized by a decay with time, which is related to the proton motions in the material. In particular, from the shape of this decay and how it depends on temperature and momentum transfer, $\hbar Q$, information about the mechanistic detail of proton motions, such as the timescale, activation energy, and spatial geometry, can be obtained.

From Fig. 9.10a, it can be seen that the $I(Q,t)$ is described well by a single exponential function (solid lines) with a relaxation time τ and a relaxation rate τ^{-1} that exhibits a Q^2-dependence (inset), which indicates that the relaxational decay is related to long-range translational diffusion. To further justify a result obtained using a single exponential function, the authors modelled the scattering function, $I_{calc.}(Q,t)$, using a kinetic model based on first-principles calculations. Figure 9.10b shows these results for momentum transfers Q = 0.3, 0.5, 2.0 $Å^{-1}$, as well as for the long-range diffusion limit $Q \rightarrow 0$, at a temperature $T = 563$ K. In the latter case, the scattering function is given by a single exponential with a characteristic relaxation rate $\tau^{-1}(Q) = DQ^2$, where D is the diffusion constant. Since the

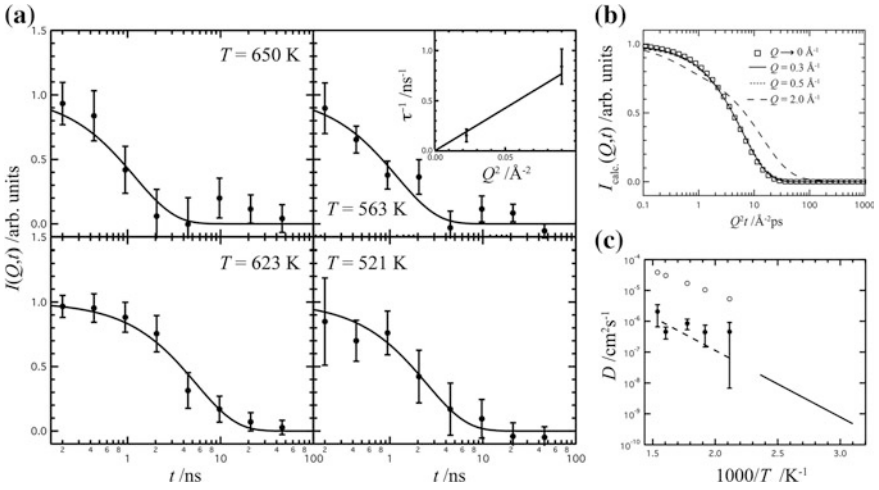

Fig. 9.10 **a** Exponential fits to $I(Q,t)$ at Q = 0.3 $Å^{-1}$ for $T = 521$–650 K. *Upper right panel* shows the Q^2-dependence of the relaxation rate at $T = 563$ K where the solid line represents a fit to $\tau^{-1} = DQ^2$, with $D = 8.53 \cdot 10^{-7}$ cm^2s^{-1}. **b** Calculated intermediate scattering-functions at $T =$ 563 K. **c** Plot of the diffusion constants obtained from NSE spectroscopy (*bullet*), first-principles calculations (*white bullet*), and conductivity measurements via the Nernst-Einstein relationship (*line*) [52]; the *dotted line* is an extrapolation of the data obtained from conductivity measurements at lower temperatures. Reprinted with permission from (M. Karlsson, D. Engberg, M.E. Björketun, A. Matic, G. Wahnström, P.G. Sundell,P. Berastegui, I. Ahmed, P. Falus, B. Farago, L. Börjesson, S. Eriksson, Chem. Mater. **22**, 740 (2010)) [65], copyright American Chemical Society

$I_{\text{calc.}}(Q,t)$s are plotted against Q^2t they collapse onto a single curve in the long-range regime and this can be seen in Fig. 9.10b up to at least Q = 0.5 Å^{-1}. These results suggest that the long-range translational diffusion of protons occurs and on this basis, a diffusion coefficient assuming a $\tau^{-1}(Q) = DQ^2$ dependence was extracted. Temperature-dependent results are shown in the Arrhenius plot in Fig. 9.10c, from which it is evident that the diffusion constant is consistent between different temperatures, showing that the analysis is physically reasonable. Included in this figure is also the diffusion constant extracted from conductivity experiments and derived from first-principles calculations. It is evident that the diffusion constant obtained from NSE and conductivity experiments are comparable, which implies that already on a length-scale as short as ~20 Å the effect of potential local traps or other "imperfections" in the structure that can be expected to affect the proton dynamics, has averaged out. That is, there are no new features revealed on a larger length-scale that have not been experienced by the proton on the shorter length-scale probed by NSE. However, by extending the Q range to higher Q values it should be possible to observe the crossover from single-exponential behaviour at low Q values, typical for long-range proton diffusion, to a more complex behaviour at larger Q values, suggesting that several processes are taking place. Further work along these lines is likely to give answers to questions like how the type and concentration of dopant atoms correlate with the macroscopic proton-conductivity, which as discussed above is a topic of some controversy.

Several researchers claim that the dopant atoms act as localized trapping-centres where the proton spends an extended time before it diffuses further throughout the material. This view was first introduced by Hempelmann et al. [32, 33] on the basis of their QENS data for $SrYb_{0.05}Ce_{0.95}O_{2.975}$, which could be described by a so-called "two-state" model, suggesting that the proton migration takes place through a sequence of trapping and release events (Fig. 9.11 (left)). This view later found support from muon spin relaxation experiments [66] and computational studies of proton dynamics in perovskite-type oxides [34, 67–70], and most recently from a combined thermogravimetric and a.c. impedance spectroscopy study [71], as well as from luminescence spectroscopy measurements [72]. Converse to this picture, Kreuer et al. [73, 74] proposed that the dopant atoms may affect the proton transport in a more nonlocal fashion (Fig. 9.11 (right)). This suggestion is based on conductivity data for Y-doped $BaCeO_3$ [73, 74], which shows that the proton conductivity increases with dopant level, but not as a result of a decrease of the pre-exponential factor, D_0, in the expression for the diffusivity $D = D_0\exp(-E_a/k_BT)$ as anticipated by the two-state model, but rather as a result of an increased activation energy, E_a [73, 74].[3] Moreover, Mulliken population analyses of the electron densities at the oxygens showed that the additional negative charge introduced by

[3] Assuming that the two-state model is true and the proton spends an average time, t_1, in the defect-free region and a time in a trap, $t_1 + t_0$, then the diffusivity is scaled by a factor, $t_1/(t_1 + t_0)$ [32]. Increasing the concentration of traps then leads to a decrease of t_1. It implies that in the two-state model the diffusivity depends on the concentration of traps but not on the activation energy.

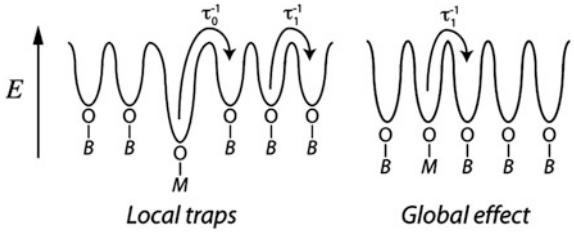

Fig. 9.11 Schematic of two different views of the potential-energy landscape experienced by the proton in hydrated $AB_{1-x}M_xO_3$ type perovskites. τ_0^{-1} and τ_1^{-1} are the escape rates from a trap and a regular oxygen site, respectively, i.e. $\tau_0^{-1} < \tau_1^{-1}$

the dopants is distributed rather homogeneously over the oxygen lattice, which results in stronger bonding of the protons with increased proton-transfer barriers in general [73].

Irrespective of whether the dopant atoms influence the proton diffusion in a spatially restricted way or more non-locally, further QENS investigations using time-of-flight, backscattering, and spin-echo methods, is likely the only way to experimentally elucidate the mechanistic detail of proton dynamics in proton-conducting perovskites. Such information is crucial for the development of strategies for the strategic design of new materials with conductivities beyond the current state-of-the-art materials and hence are critical for future breakthroughs in the development of intermediate-temperature fuel-cell technology.

9.3.4 Neutron Prompt-Gamma Activation Analysis

In order to make correct statements about the role of protons and oxygen vacancies on the structure and dynamics of proton-conducting oxides, an accurate measure of the proton concentration in the material is necessary. Determinations of proton concentrations are done routinely using thermogravimetric methods by measuring the weight change of the sample during dehydration on heating [26]. However, the use of thermogravimetric methods is not suitable for all types of materials. For example, hydrated perovskites containing elements that may change oxidation state upon heating may decrease in mass because of oxygen loss in addition to the evaporation of water molecules. An alternative technique for the analysis of proton concentration in such systems is neutron prompt-gamma activation analysis (PGAA), which can indeed be used for determining the presence and amount of elements in materials, irrespective of oxidation state.

An example of a PGAA study of a proton-conducting perovskite is the work by Jones et al. [75] on undoped and Y-doped $BaPrO_3$. The PGAA spectra of dry and hydrated (saturated) $BaY_{0.1}Pr_{0.9}O_{3-\delta}$ are shown in Fig. 9.12a. The sensitivity to hydrogen and the effect of hydration are clearly visible. The proton concentration,

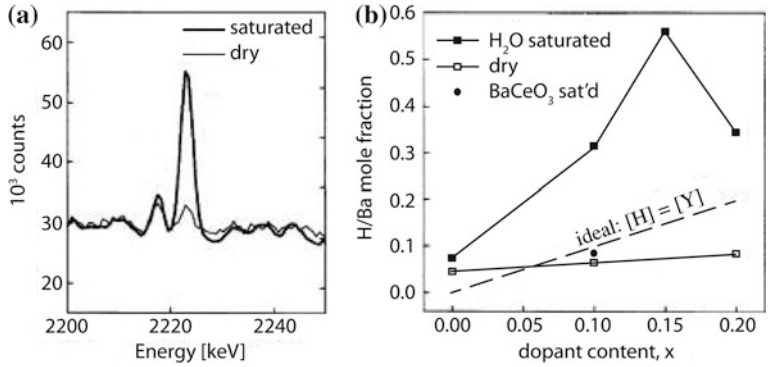

Fig. 9.12 **a** Neutron PGAA spectra of dry and hydrated (saturated) $BaY_{0.1}Pr_{0.9}O_{3-\delta}$. **b** Proton concentration in dry (*white squares*) and hydrated (*black squares*) $BaY_{0.1}Pr_{0.9}O_{3-\delta}$, determined from the PGAA spectra. A comparison with hydrated $BaY_{0.1}Ce_{0.9}O_{3-\delta}$ (*bullets*) is included. The figure is modified and reprinted with permission from (C.Y. Jones, J. Wu, L. Li, S.M. Haile, J. Appl. Phys. **97**, 114908 (2005)) [75], copyright American Institute of Physics

as derived from the PGAA spectra, is shown in Fig. 9.12b for both samples. A key result of this study is that the proton concentration in the hydrated Y-doped $BaPrO_3$ sample is as much as three times larger than the dopant concentration. The unexpectedly-high proton concentration in the hydrated sample is thought to occur as a result of the change of the Pr oxidation state from +4 to +3. This implies that the Pr ions act as self-dopants, which form intrinsic oxygen-vacancies that add to the oxygen vacancies formed by the replacement of Pr for Y. Hence, the material can accommodate more −OH groups and therefore take up more protons than is expected from the dopant concentration alone. This information is naturally of paramount importance for making the correct analysis and conclusions from data obtained in both structural and dynamical studies.

9.4 Case Studies of Other Classes of Proton-Conducting Ceramics

It is clear that research on proton-conducting ceramics continues to be focused on archetypical ABO_3-type perovskites. However, a variety of other classes of proton-conducting ceramics which show appreciable proton-conductivities at intermediate to high temperatures have been developed, and are receiving increased attention. Examples of these include more complex perovskites of the form $Ba_3Ca_{1.18}Nb_{1.82}O_{8.72}$ and $Sr_3CaZr_{0.5}Ta_{1.5}O_{8.75}$ [19–21], which possess cation ordering leading to a doubling of the unit-cell, and perovskite-related phases such as brownmillerite-structured oxides (e.g. $Ba_2In_2O_5$ [49]). Other examples include gallium-based oxides (e.g. $LaBaGaO_4$ [76]), pyrochlores (e.g. $La_2Zr_2O_7$ [23, 24]),

phosphates (e.g. $LaPO_4$ [77, 78]), niobates and tantalates (e.g. $LaNbO_4$ [79]), tungstates (e.g. La_6WO_{12} [80]), solid acids (e.g. $CsHSO_4$ [81]), hydrated alkali thio-hydroxogermanates (e.g. $Cs_2GeS_2(OH)_2{\cdot}yH_2O$ [16, 82]), tungsten-bronze titanate/niobate systems (e.g. $Ba_{0.6}Mg_{0.067}Nb_{0.933}O_3$ [83]), and cupsidine systems (e.g. $La_4(Ga_{2-x}Ti_xO_{7+x/2})O_2$, $x = 0$–2 [84]).

In this section, we follow some examples of recent neutron-scattering studies of hydrated alkali thio-hydoxogermanates, solid acids, and gallium-based oxides, to further highlight the breath of information that can be obtained with neutron scattering.

9.4.1 ND Study of Hydrated Alkali Thio-Hydroxogermanates

Hydrated alkali thio-hydroxogermanates, $M_xGeS_x(OH)_{4-x}{\cdot}yH_2O$, where M = Na, K, Rb or Cs; $1 < x < 4$; $y \sim 1$, represent a novel class of amorphous proton-conducting materials, which were first synthesized by Poling et al. [16, 82] at Iowa State University. The conductivities of these materials typically reach a maximum of the order of 10^{-2} Scm^{-1} in the intermediate-temperature range of 100–300 °C [16], which competes with even the best perovskite-type oxides. Karlsson et al. [85] reported a structural investigation of these materials using a combination of neutron diffraction and first-principles calculations. A key result from the experiment was that the neutron structure-factors of the hydrated and dehydrated materials (Fig. 9.13) are overall similar to each other, indicating that there are no dramatic structural changes such as phase transitions or structure degradation as the materials are dehydrated. In order to gain understanding for what such a structure may look like, the authors proceeded their analysis by generating a candidate three-dimensional structure of the Cs-based compound, by taking the orthorhombic crystal structure of $Na_2GeS_2(OH)_2{\cdot}5H_2O$ as the starting point in the calculations, replacing the Na ions with Cs ions and reducing the number of water molecules from five to one in order to agree with the real composition. Snapshots of the generated structures of dehydrated and hydrated materials are shown in Fig. 9.14, whereas Fig. 9.15 shows a close up of the local configuration of the hydrated material.

In the hydrated state (Figs. 9.14a and 9.15), the calculations suggest a structure built of thio-hydroxogermanate anion dimers connected to each other via hydrogen bonds to water molecules located between the dimers. In the dehydrated state (Fig. 9.14b), the calculations suggest instead that the thio-hydroxogermanate anions form an extended network through the creation of inter-dimer hydrogen bonds, whereas the alkali ions are found to act as "space fillers" in "voids" formed by the thio-hydroxogermanate anion dimers in both the hydrated and dehydrated state. These generated structures are justified by comparing the experimental and calculated pair-correlation functions, which are shown in Fig. 9.16. It can be appreciated that the experimental and calculated pair-correlation functions are overall similar

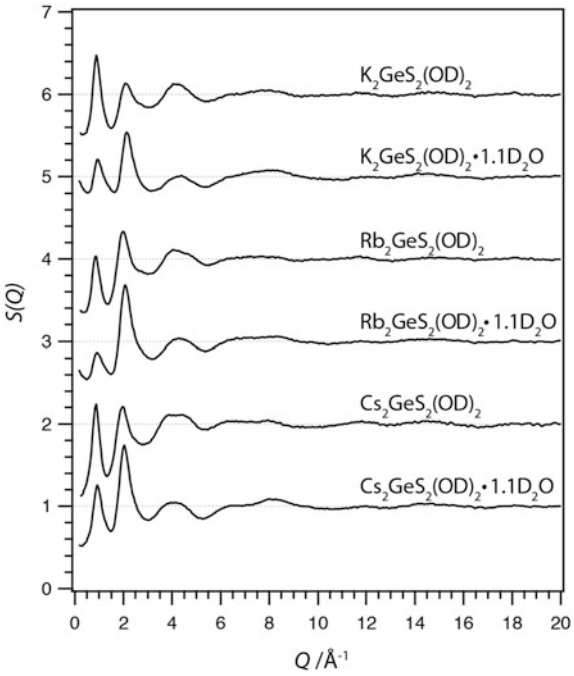

Fig. 9.13 Experimental neutron static structure-factors of hydrated and dehydrated $Cs_2GeS_2(OD)_2{\cdot}yD_2O$, $Rb_2GeS_2(OD)_2{\cdot}yD_2O$, and $K_2GeS_2(OD)_2{\cdot}yD_2O$. For clarity, the diffractograms have been vertically shifted by unity. The figure is reprinted with permission from (M. Karlsson, A. Matic, I. Panas, D.T. Bowron, S.W. Martin, C.R. Nelson, C.A. Martindale,A. Hall, L. Börjesson, Chem. Mater. **20**, 6014 (2008)) [85], copyright American Chemical Society

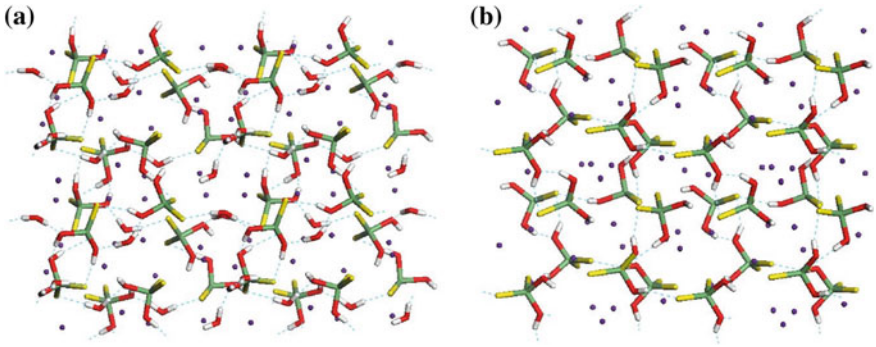

Fig. 9.14 Snapshots of the modelled structure of **a** Hydrated and **b** Dehydrated $Cs_2GeS_2(OH)_2{\cdot}yH_2O$ [85]. Oxygen is shown in *red*, sulfur in *yellow*, hydrogen in *white*, and cesium in *violet*. *Dashed lines* are hydrogen bonds. The figure is reprinted with permission from (M. Karlsson, A. Matic, I. Panas, D.T. Bowron, S.W. Martin, C.R. Nelson, C.A. Martindale,A. Hall, L. Börjesson, Chem. Mater. **20**, 6014 (2008)) [85], copyright American Chemical Society

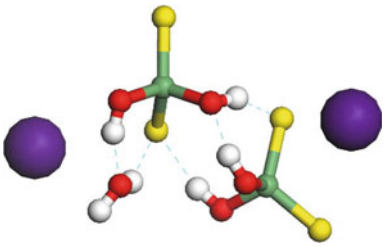

Fig. 9.15 Part of the $Cs_2GeS_2(OH)_2{\cdot}yH_2O$ structure obtained from modelling [85]. Oxygen is *red*, sulfur is *yellow*, hydrogen is *white*, and cesium and germanium ions are *violet* and *green*, respectively. *Dashed lines* are hydrogen bonds. The figure is reprinted with permission from (M. Karlsson, A. Matic, I. Panas, D.T. Bowron, S.W. Martin, C.R. Nelson, C.A. Martindale,A. Hall, L. Börjesson, Chem. Mater. **20**, 6014 (2008)) [85], copyright American Chemical Society

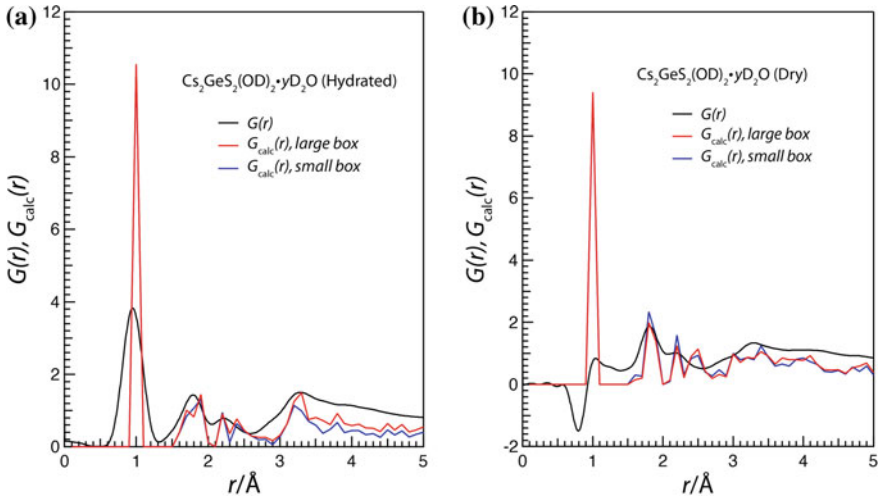

Fig. 9.16 Comparison of pair-correlation functions for **a** Hydrated and **b** Dehydrated $Cs_2GeS_2(OD)_2{\cdot}yD_2O$, obtained from ND and first-principles calculations. *Red* depicts the larger and *blue* the smaller, computational boxes. The figure is reprinted with permission from (M. Karlsson, A. Matic, I. Panas, D.T. Bowron, S.W. Martin, C.R. Nelson, C.A. Martindale,A. Hall, L. Börjesson, Chem. Mater. **20**, 6014 (2008)) [85], copyright American Chemical Society

which suggests that the real structures are at least reasonably-well described by the structural models for both the hydrated and dehydrated materials. However, to obtain a complete picture of the structure and elucidate how the structure depends on the type and concentration of alkali ion, further investigations, such as reverse Monte-Carlo simulations of diffraction data, are necessary.

9.4.2 QENS Study of Nanoionic Proton-Mobility in Solid Acids

Proton-conducting solid acids are compounds, such as $KHSO_4$ and $CsHSO_4$, that feature spectacular phase transitions during heating for which the proton conductivity increases by several orders of magnitude [81, 86, 87]. $CsHSO_4$, for example, has a phase-transition temperature of 414 K [81]. Below this temperature, $CsHSO_4$ has a monoclinic structure in which the number of protons is equal to the number of proton sites. Consequently, the hydrogen atoms are localized within rigid hydrogen bonds between SO_4 tetrahedra and hence their mobility is low. In the high-temperature phase, the SO_4 tetrahedra can rotate rather freely between crystallographically identical positions, creating six times as many possible proton sites as there are protons available. As a result, an almost isotropic and dynamic hydrogen-bonding network between the different sulfate groups is created, where all oxygens are involved in hydrogen bonding. In this hydrogen-bonded network, proton diffusion is a fast process which occurs through proton jumps between neighbouring SO_4 groups, as assisted by rotational motion of these groups.

Chan et al. [88] addressed the question of how the addition of nanoparticles, such as SiO_2 and TiO_2, impacts on the $CsHSO_4$ phase-transition temperature and proton conductivity. Using QENS the authors showed that nanostructuring has the twin effect of lowering the superprotonic phase-transition temperature and increasing the local diffusional-dynamics in the superprotonic phase. The results are summarized in Fig. 9.17, which shows (a) the QENS spectra of bulk $CsHSO_4$ and nanocomposite $CsHSO_4$ with SiO_2 (7 nm), (b) the quasielastic width, and (c) the fraction of mobile protons as derived from the quasielastic intensity as a function of temperature. As can be seen in Fig. 9.17b, the phase-transition temperature for the nanostructured

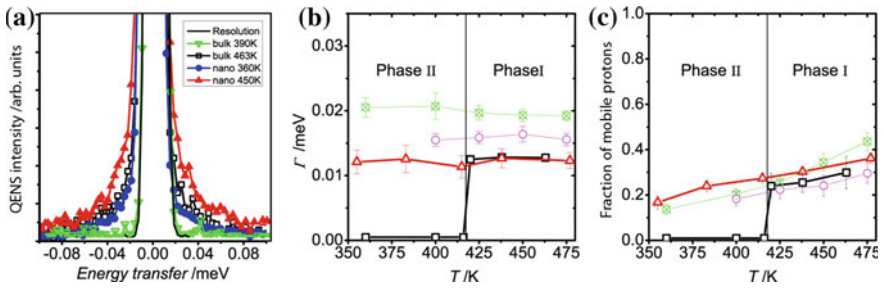

Fig. 9.17 **a** QENS spectra of bulk $CsHSO_4$ and SiO_2 (7 nm) nanocomposite samples with molar ratio 1:2 at $Q = 0.61$ Å^{-1}. **b** Width of the quasielastic signal, Γ, as related to proton mobility at $Q = 1$ Å^{-1} for four different samples. **c** Fraction of mobile protons derived from the integrated intensity of the quasielastic scattering. *Black squares* bulk $CsHSO_4$, *red triangles* nanocomposite $CsHSO_4$ with 24 nm TiO_2 particles, *purple circles* nanocomposite $CsHSO_4$ with 40 nm SiO_2 particles, *green hexagons* nanocomposite $CsHSO_4$ with 7 nm SiO_2 particles. The figure is reprinted with permission from (W.K. Chan, L.A. Haverkate, W.J.H. Borghols, M. Wagemaker, S. J. Picken, E.R.H. van Eck,A.P.M. Kentgens, M.R. Johnson, G.J. Kearley, F.M. Mulder, Adv. Funct. Mater. **21**, 1364 (2011)) [88], copyright Wiley

samples is reduced to a least 360 K. As suggested by Chan et al. [88], this behaviour may be linked to the creation of space-charge layers between the conducting phases and the nanoparticles. The creation of such space-charge layers would lead to an increase of the number of vacant sites for the protons to move to, hence allowing a larger fraction of the protons to become as mobile as they are in the superprotonic phase. Indeed, Fig. 9.17c shows that up to 25 % of the protons are mobile in the nanocomposite sample below the phase-transition temperature of 414 K, whereas no sign of proton mobility can be seen in the bulk sample at those temperatures. The results suggest that nanostructuring may be a rewarding research direction in the pursuit of optimized proton-conductivity.

9.4.3 ND Studies of Structure and Proton Sites in Lanthanum Gallates

Lanthanum barium gallates, i.e. $LaBaGaO_4$-based compounds, represent a novel class of proton-conducting oxides [89]. The structure of these materials consists of discrete GaO_4 tetrahedra which are charge balanced by Ba/La ions, as shown in Fig. 9.18a. Increasing the Ba:La ratio results in the formation of oxygen vacancies, and similarly to perovskite-type oxides, such vacancies can be filled with −OH groups in a humid atmosphere [89]. In this regard, Kendrick et al. [89] raised the question of how the oxygen vacancies are accommodated in the structure, with the knowledge that the inclusion of oxygen vacancies may result in energetically unfavourable three-coordinated Ga atoms, which would limit the oxygen vacancy concentration and hence the degree of hydration. Using computer-modelling methods, the authors found that the oxygen vacancies are accommodated via considerable relaxation of neighbouring GaO_4 tetrahedra, resulting in the formation of

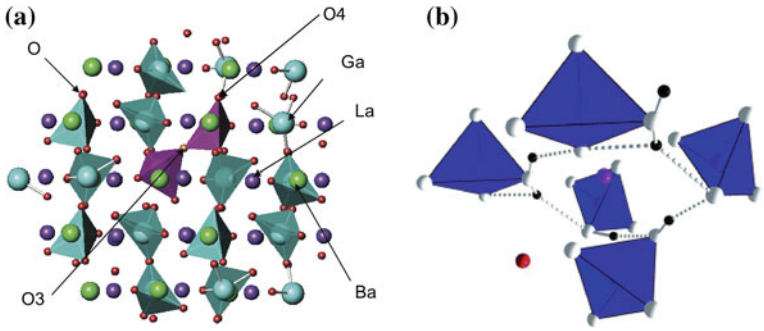

Fig. 9.18 **a** Crystal structure of $LaBaGaO_4$, illustrating tetrahedrally coordinated Ga and the presence of Ga_2O_7 units (*purple*). The figure is taken from Ref. [90] **b** Hydrogen-bonding interactions in $La_{0.8}Ba_{1.2}GaO_{3.96}H_{0.12}$. *Tetrahedra* GaO_4, *pink sphere* La, *red sphere* Ba, *white spheres* O, *black spheres* H. The figure is reprinted with permission from Ref. (E. Kendrick, K.S. Knight, M.S. Islam, P.R. Slater, J. Mater. Chem. **20**, 10412 (2010)) [91], copyright The Royal Society of Chemistry

Ga_2O_7 groups so that the Ga retains tetrahedral coordination (see purple unit in Fig. 9.18a) [89]. These computational results were supported by ND results which showed a splitting of the oxygen site, consistent with the presence of both GaO_4 and Ga_2O_7 [89]. Hydration of the material can lead to the breaking of such units [89].

On the basis of these results, later investigations focussed on proton positions within the hydrated form of the lanthanum barium gallate structure, using ND coupled with difference Fourier-density analysis of protonated and deuterated samples. Notably, three stable proton positions, one located adjacent to the O3 site and two located adjacent to the O4 site, were found (Fig. 9.18a). The presence of several proton sites is in agreement with modelling work suggesting little difference in energy between proton sites for different oxygens [89]. Further, determination of Ga–O–H bond angles indicated that protons point almost perpendicularly to the Ga–O bond direction and that the protons experience a mixture of intra- and inter-tetrahedral hydrogen-bonding, as shown in Fig. 9.18b [91]. The highest degree of hydrogen bonding is found for O3–H···O3 linkages, in agreement with previous modelling work [91]. Modelling also suggests facile inter-tetrahedron proton-conducting pathways due to hydrogen bonding, whereas intra-tetrahedron pathways are found to be less favourable and hence rate-limiting for proton conduction [89].

9.5 Prospectives of Future Proton-Conducting Ceramics Research

Independent of the direction of future research, a major leap in the development of next-generation fuel cells depends on the exploration of new classes of materials and a better understanding of those already known. This chapter has given a flavour of past and current research in the area of proton-conducting ceramics, targeted as electrolytes for future intermediate-temperature fuel-cell technology, and demonstrated the important role neutron scattering plays in elucidating the fundamental science of these materials. In particular, a collection of contemporary neutron studies on proton-conducting perovskite type oxides, hydrated alkali thio-hydroxogermanates, solid acids, and gallium-based oxides, using a range of different neutron methods, has been reviewed in order to illustrate the breadth of information that can be obtained.

In the future, it is clear that there exists great scope for further neutron studies to explore and understand the basic science of structural and dynamical aspects of such classes of proton-conducting oxides. In particular, I foresee an increasing use of PDF analysis and reverse Monte-Carlo modelling [92, 93] of neutron total-scattering data for the investigation (and re-investigation) of local-structural details, such as bond distances and angles, proton sites, and oxygen vacancy and/or cation ordering, for example, of both traditional and new materials. The influence of interactions between oxygen vacancies and dopant atoms on the conductivity of

oxide-ion conducting yttria-doped zirconia has been observed [94, 95] and their extension to the broader class of proton-conducting perovskite-structured analogues is an interesting direction of research. In parallel, QENS will play an increasingly important role in elucidating the detail of the proton-conduction mechanism and how it depends on the local-structural details as explored with diffraction methods. For this purpose, I foresee an increasing use of the neutron spin-echo technique in particular, which offers the twin advantages of reaching the long time-scales needed to observe the translational proton-diffusion on an atomic length-scale whilst covering a very large time-range, so that it may be possible to observe and analyse different types of proton motions in a single measurement.

The importance of exploring nanoionic and thin film phenomena is also noted, as nanostructuring and thin film properties may be, and often are, different from the properties of the bulk. In this context, the use of neutron reflectivity, a technique which, to the best of my knowledge, thus far has been neglected in studies of proton-conducting oxides, offers unique possibilities to obtain information about surface and near-surface states and may yield information such as the properties of interfaces and distribution of protons across a single electrolytic-membrane or membrane-electrode assembly. Such information would certainly help in understanding the role of interfaces and, in particular, the reason for the reduced proton conductivity across grain boundaries (GBs). Two explanations for low GB conductivity have been put forward, the first being a structural misalignment in the GB region, and the second being the appearance of a space-charge layer around the GB core, leading to Schottky barriers and the depletion of mobile protons. Presently, the latter explanation predominates research [96, 97], however, details of the GB core are neither well understood nor sufficiently explored.

From a more technical point of view, the recent development of in situ conductivity and humidification cells for ND now allow relatively small features in conductivity to be related to concurrent changes in structure and/or level of hydration [98]. In the near future, the development of in situ cells may also enable investigations of materials under conditions that mimic those under operating fuel-cell conditions and therefore also present the potential to bridge the gap between fundamental scientific problems and applied research. In the longer term, this research can expect also to benefit from the development of completely-new instrumental concepts. An example of this is the recent demonstration of using dynamic nuclear-polarization techniques [99] coupled with ND, where the Bragg peaks can be enhanced or diminished significantly and the incoherent background is reduced [100]. This method offers unique possibilities to tune continuously the contrast of the Bragg reflections and thereby represents a new tool for increasing substantially the signal-to-noise ratio in ND patterns of hydrogenous matter, including proton-conducting oxides.

9.6 Concluding Remarks

This chapter has aimed to demonstrate the valuable role that neutron scattering now plays in providing deeper insight into the fundamental aspects of structure and dynamics of proton-conducting ceramics, with a view to their implementation as electrolytes in next-generation intermediate-temperature fuel cells. Future research in this area is likely to include new challenges with respect to key fundamental properties such as the mechanistic detail of average crystal-structures, local-structural disorder, hydrogen-bonding interactions, proton dynamics, proton incorporation, and nanoionic phenonmena, in archetypical proton-conducting perovskite type oxides as well as in more modern classes of proton conductors.

Acknowledgments Financial support from the Swedish Research Council (Grant no. 2011-4887) is gratefully acknowledged. P. Slater is thanked for the provision of Fig. 9.18a.

References

1. B.C.H. Steele, A. Heinzel, Nature **414**, 345 (2001)
2. D.J.L. Brett, A. Atkinson, N.P. Brandon, S.J. Skinner, Chem. Soc. Rev. **37**, 1568 (2008)
3. A. Orera, P.R. Slater, Chem. Mater. **22**, 675 (2010)
4. A.J. Jacobson, Chem. Mater. **22**, 660 (2010)
5. J.A. Kilner, Faraday Discuss. **134**, 9 (2007)
6. V.V. Kharton, F.M.B. Marques, A. Atkinson, Solid State Ionics **174**, 135 (2004)
7. H.L. Tuller, Phys. Chem. Chem. Phys. **11**, 3023 (2009)
8. N.Q. Minh, Solid State Ionics **174**, 271 (2004)
9. J.B. Goodenough, Annu. Rev. Mater. Res. **33**, 91 (2003)
10. L. Carrette, K.A. Friedrich, U. Stimming, ChemPhysChem **1**, 162 (2000)
11. J. Larminie, A. Dicks, *Fuel Cell Systems Explained*, 2nd edn. (Wiley, new York, 2003)
12. A. Weber, E. Ivers-Tiffée, J. Power Sources **127**, 273 (2004)
13. K.D. Kreuer, J. Membr. Sci. **185**, 29 (2001)
14. E. Traversa, Electrochem. Soc. Interface **18**, 49 (2009)
15. K.D. Kreuer, ChemPhysChem **3**, 771 (2002)
16. S. Poling, C. Nelson, S.W. Martin, Chem. Mater. **17**, 1728 (2005)
17. M. Karlsson, Dalton Trans. **42**(2), 317 (2013)
18. H. Iwahara, T. Esaka, H. Uchida, N. Maeda, Solid State Ionics **3–4**, 359 (1981)
19. K.C. Liang, A.S. Nowick, Solid State Ionics **61**, 77 (1993)
20. K.C. Liang, Y. Du, A.S. Nowick, Solid State Ionics **69**, 117 (1994)
21. H.G. Bohn, T. Schober, T. Mono, W. Shilling, Solid State Ionics **117**, 219 (1999)
22. Y. Larring, T. Norby, Solid State Ionics **77**, 147 (1995)
23. T. Shimura, M. Kumori, H. Iwahara, Solid State Ionics **86–88**, 685 (1996)
24. T. Omata, K. Okuda, S. Tsugimoto, S. Otsuka-Yao-Matsuo, Solid State Ionics **104**, 249 (1997)
25. V.M. Goldschmidt, Naturwissenschaften **14**, 477 (1926)
26. K.D. Kreuer, Ann. Rev. Mater. Res. **33**, 333 (2003)
27. F.A. Kröger, H.J. Vink, *Solid State Physics: Advances in Research and Applications* (Academic Press, New York, 1956)
28. W. Münch, G. Seifert, K.D. Kreuer, J. Maier, Solid State Ionics **97**, 39 (1997)
29. K.D. Kreuer, W. Munch, U. Traub, J. Maier, Ber. Bunsenges. Phys. Chem. **102**, 552 (1998)

30. W. Münch, G. Seifert, K.D. Kreuer, J. Maier, Solid State Ionics **86–88**, 647 (1996)
31. F. Shimojo, K. Hoshino, H. Okazaki, J. Phys. Soc. Jpn. **66**, 8 (1997)
32. R. Hempelmann, C. Karmonik, T. Matzke, M. Cappadonia, U. Stimming, T. Springer, M.A. Adams, Solid State Ionics **77**, 152 (1995)
33. T. Matzke, U. Stimming, C. Karmonik, M. Soetramo, R. Hempelmann, F. Güthoff, Solid State Ionics **86–88**, 621 (1996)
34. M.S. Islam, R.A. Davies, J.D. Gale, Chem. Mater. **13**, 2049 (2001)
35. H.G. Bohn, T. Schober, J. Am. Ceram. Soc. **83**, 768 (2000)
36. P. Babilo, S.M. Haile, J. Am. Ceram. Soc. **88**, 2362 (2005)
37. F.M.M. Snijkers, A. Buekenhoudt, J. Cooymans, J.J. Luyten, Scripta Mater. **50**, 655 (2004)
38. P. Babilo, T. Uda, S.M. Haile, J. Mater. Res. **22**, 1322 (2007)
39. S. Tao, J.T.S. Irvine, Adv. Mat. **18**, 1581 (2006)
40. N. Ito, H. Matsumoto, Y. Kawasaki, S. Okada, T. Ishihara, Solid State Ionics **179**, 324 (2008)
41. S. Imashuku, T. Uda, Y. Nose, K. Kishida, S. Harada, H. Inui, Y. Awakura, J. Electrochem. Soc. **155**, B581 (2008)
42. K.S. Knight, Solid State Ionics **127**, 43 (2000)
43. N. Sata, K. Hiramotom, M. Ishigame, S. Hosoya, N. Niimura, S. Shin, Phys. Rev. B **54**, 15795 (1996)
44. I. Sosnowska, R. Prezenioslo, W. Schafer, W. Kockelmann, R. Hempelmann, K. Wysocki, J. Alloy Compd. **328**, 226 (2001)
45. E. Kendrick, K.S. Knight, M.S. Islam, P.R. Slater, Solid State Ionics **178**, 943 (2007)
46. I. Ahmed, C.S. Knee, M. Karlsson, S.G. Eriksson, P.F. Henry, A. Matic, D. Engberg, L. Börjesson, J. Alloy Compd. **450**, 103 (2008)
47. A.K. Azad, J.T.S. Irvine, Chem. Mater. **21**, 215 (2009)
48. M. Karlsson, M.E. Björketun, P.G. Sundell, A. Matic, G. Wahnström, D. Engberg, L. Börjesson, I. Ahmed, S.G. Eriksson, P. Berastegui, Phys. Rev. B **72**, 1 (2005)
49. P. Berastegui, S. Hull, F.J. García-García, S.-G. Eriksson, J. Solid State Chem. **164**, 119 (2002)
50. L. Malavasi, H.J. Kim, T. Proffen, J. Appl. Phys. **9**, 2309 (2008)
51. L. Malavasi, H.J. Kim, T. Proffen, J. Appl. Phys. **105**, 123519 (2009)
52. K.D. Kreuer, S. Adams, W. Münch, A. Fuchs, U. Klock, J. Maier, Solid State Ionics **145**, 295 (2001)
53. C. Karmonik, T.J. Udovic, R.L. Paul, J.J. Rush, K. Lind, R. Hempelmann, Solid State Ionics **109**, 207 (1998)
54. T. Yildrim, B. Reisner, T.J. Udovic, D.A. Neumann, Solid State Ionics **145**, 429 (2001)
55. M. Karlsson, A. Matic, S.F. Parker, I. Ahmed, L. Börjesson, S.G. Eriksson, Phys. Rev. B **77**, 104302 (2008)
56. M. Karlsson, A. Matic, C.S. Knee, I. Ahmed, L. Börjesson, S.G. Eriksson, Chem. Mater. **20**, 3480 (2008)
57. M.E. Björketun, P.G. Sundell, G. Wahnström, D. Engberg, Solid State Ionics **176**, 3035 (2005)
58. G.L. Squires, *Introduction to the Theory of Thermal Neutron Scattering* (Cambridge University Press, Cambridge, 1978)
59. M. Pionke, T. Mono, W. Schweika, T. Springer, H. Schober, Solid State Ionics **97**, 497 (1997)
60. A. Braun, S. Duval, P. Ried, J. Embs, F. Juranyi, T. Strässle, U. Stimming, R. Hempelmann, P. Holtappels, T. Graule, J. Appl. Electrochem. **39**, 262103 (2009)
61. B. Groß, C. Beck, F. Meyer, T. Krajewski, R. Hempelmann, H. Altgeld, Solid State Ionics **145**, 325 (2001)
62. D. Wilmer, T. Seydel, K.D. Kreuer, Mater. Res. Soc. Proc. **972**, 15 (2007)
63. P. Colomban, A. Slodszyk, D. Lamago, G. Andre, O. Zaafrani, O. Lacroix, S. Willemin, B. Sala, J. Phys. Soc. Jpn. **79**, 1 (2010)
64. M. Karlsson, A. Matic, D. Engberg, M.E. Björketun, M.M. Koza, I. Ahmed, G. Wahnström, P. Berastegui, L. Börjesson, S.G. Eriksson, Solid State Ionics **180**, 22 (2009)

65. M. Karlsson, D. Engberg, M.E. Björketun, A. Matic, G. Wahnström, P.G. Sundell, P. Berastegui, I. Ahmed, P. Falus, B. Farago, L. Börjesson, S. Eriksson, Chem. Mater. **22**, 740 (2010)
66. R. Hempelmann, M. Soetratmo, O. Hartmann, R. Wäppling, Solid State Ionics **107**, 269 (1998)
67. R.A. Davies, M.S. Islam, J.D. Gale, Solid State Ionics **126**, 323 (1999)
68. M.S. Islam, P.R. Slater, J.R. Tolchard, T. Dinges, Dalton Trans. 3061 (2004)
69. M.E. Björketun, P.G. Sundell, G. Wahnström, Faraday Discuss. **134**, 247 (2007)
70. M.E. Björketun, P.G. Sundell, G. Wahnström, Phys. Rev. B: Condens. Matter **76**, 054307 (2007)
71. Y. Yamazaki, F. Blanc, Y. Okuyama, L. Buannic, J.C. Lucio-Vega, C.P. Grey, S.M. Haile, Nature Mater. **12**, 647 (2013)
72. P. Haro-Gonzáles, M. Karlsson, S. Gaita, C.S. Knee, M. Bettinelli, Solid State Ionics **247–248**, 94 (2013)
73. K.D. Kreuer, W. Münch, M. Ise, T. He, A. Fuchs, U. Traub, J. Maier, Ber. Bunsenges. Phys. Chem. **101**, 1344 (1997)
74. K.D. Kreuer, Solid State Ionics **125**, 285 (1999)
75. C.Y. Jones, J. Wu, L. Li, S.M. Haile, J. Appl. Phys. **97**, 114908 (2005)
76. F. Schönberger, E. Kendrick, M.S. Islam, P.R. Slater, Solid State Ionics **176**, 2951 (2005)
77. K. Amezawa, H. Maekawa, Y. Tomii, N. Yamamoto, Solid State Ionics **145**, 233 (2001)
78. N. Kitamura, K. Amezawa, Y. Tomii, N. Yakamoto, Solid State Ionics **162–163**, 161 (2003)
79. R. Haugsrud, T. Norby, Nat. Mater. **5**, 193 (2006)
80. A. Magraso, C. Frontera, D. Marrero-López, P.Núñez, Dalton Trans. **10**, 283 (2009)
81. S.M. Haile, D.A. Boysen, C.R.I. Chisholm, R.B. Merle, Nature **410**, 910 (2001)
82. S.A. Poling, C.R. Nelson, S.W. Martin, Mater. Lett. **60**, 23 (2006)
83. E. Kendrick, M.S. Islam, P.R. Slater, Solid State Ionics **176**, 2975 (2005)
84. M.C. Martin-Sedeno, D. Marrero-Lopez, E.R. Losilla, L. Leon-Reina, S. Bruque, P. Núñez, M.A.G. Aranda, Chem. Mater. **17**, 5989 (2005)
85. M. Karlsson, A. Matic, I. Panas, D.T. Bowron, S.W. Martin, C.R. Nelson, C.A. Martindale, A. Hall, L. Börjesson, Chem. Mater. **20**, 6014 (2008)
86. T. Norby, Nature **410**, 877 (2001)
87. A.I. Baranov, L.A. Shuvalov, N.M. Schagina, JETP LETT. **36**, 459 (1982)
88. W.K. Chan, L.A. Haverkate, W.J.H. Borghols, M. Wagemaker, S.J. Picken, E.R.H. van Eck, A.P.M. Kentgens, M.R. Johnson, G.J. Kearley, F.M. Mulder, Adv. Funct. Mater. **21**, 1364 (2011)
89. E. Kendrick, J. Kendrick, K.S. Knight, M.S. Islam, P.R. Slater, Nat. Mater. **6**, 871 (2007)
90. E. Kendrick, P.R. Slater, University of Surrey Chemistry Electronic Publication Library, http://epubs.surrey.ac.uk/1685 (2010)
91. E. Kendrick, K.S. Knight, M.S. Islam, P.R. Slater, J. Mater. Chem. **20**, 10412 (2010)
92. R.L. McGreevy, L. Pusztai, Mol. Simul. **1**, 359 (1988)
93. R.L. McGreevy, J. Phys.: Condens. Mat. **13**, 4111 (2001)
94. S.T. Norberg, S. Hull, I. Ahmed, S.G. Eriksson, D. Marrocchelli, P.A. Madden, P. Li, J.T.S. Irvine, Chem. Mater. **23**, 1356 (2011)
95. D. Marrocchelli, P.A. Madden, S.T. Norberg, S. Hull, Chem. Mater. **23**, 1365 (2011)
96. C.T. Chen, C.E. Danel, S. Kim, J. Mater. Chem. **21**, 5435 (2011)
97. M. Shirpour, R. Merkle, C.T. Lin, J. Maier, Phys. Chem. Chem. Phys. **14**, 730 (2012)
98. F.G. Kinyanjui, S.T. Norberg, I. Ahmed, S.G. Eriksson, S. Hull, Solid State Ionics **225**, 312 (2012)
99. A. Abragam, M. Goldman, *Nuclear Magnetism, Order and Disorder* (Oxford University Press, Oxford, 1961)
100. F.M. Piegsa, M. Karlsson, B. van den Brandt, C.J. Carlile, E.M. Forgan, P. Hautle, J.A. Konter, G.J. McIntyre, O. Zimmer, J. Appl. Cryst. **46**, 30 (2013)